Electromagnetic-thermal Coupled Analyses and Joint Optimisation of Electrically-excited Flux-switching Linear Machines

Hui Wen, *Member, IEEE*, Yufei Wang, Yuting Zheng, *Member, IEEE*, Wen Zeng, Xiao Qu, and Jiongjiong Cai

Abstract—Electrically-excited flux-switching machines are advantageous in simple and reliable structure, good speed control performance, low cost, etc., so they have arouse wide concerns from new energy field. However, they have much lower torque density/thrust density compared with the same type PM machines. To overcome this challenge, electromagnetic-thermal coupled analysis is carried out with respect to water-cooled electrically-excited flux-switching linear machines (EEFSLM).

The simulation results indicate that the conventional fixed copper loss method (FCLM) is no longer suitable for high thrust density design, since it is unable to consider the strong coupling between the electromagnetic and thermal performance. Hence, a multi-step electromagnetic-thermal joint optimisation method is proposed, which first ensures the consistency between the electromagnetic and thermal modelling and then considers the effect of different field/armature coil sizes. By using the proposed joint optimisation method, it is found that the combination of relatively large size of field coil and relatively low field copper loss is favourable for achieving high thrust force for the current EEFSLM design. Moreover, the thrust force is raised by 13-15% compared with using the FCLM. The electromagnetic and thermal performance of the EEFSLM is validated by the prototype test.

Index Terms—Electrically-excited flux-switching linear machine (EEFSLM), Thrust density, Electromagnetic-thermal coupled analysis, Joint optimisation, coil size, copper loss.

I. INTRODUCTION

IN recent years, the rapid development of new energy industry, such as electric vehicles, wind power generation and wave power generation, has been continuously boosting the demand of high performance of electrical machines[1]-[3]. For example, the competitive electric vehicle market entails light weight, miniaturization and high efficiency of electrical machines for driving and servo control applications. Under this

Hui Wen, Yufei Wang, Yuting Zheng, Wen Zeng, Xiao Qu and Jiongjiong Cai are with School of Automation and Electrical Engineering, Zhejiang University of Science and Technology, Hangzhou, China and are also with Key Institute of Robotics Industry of Zhejiang Province, Hangzhou, China (email: whhh@zust.edu.cn, 222007855042@zust.edu.cn, yutingzheng@zust.edu.cn, 1210320026@zust.edu.cn, quxiao@zust.edu.cn, caijj@zust.edu.cn).
(Corresponding Author: Jiongjiong Cai)

background, flux-switching permanent-magnet machines (FSPMMs), which has outstanding advantages of high torque density, simple rotor structure and good anti-demagnetization ability[4]-[6], have arouse wide concerns from both academic and industrial fields. Many scholars have carried out research in the topics of working principle[7][8], pole-slot combination[9][10], winding configuration[11][12], modular stator/rotor structures[13][14], cooling methods[15][16], aiming at achieving higher power density, stronger fault-tolerant ability and better speed adjustment performance. In particular, linear FSPMM is especially suitable for long-stroke application, as it completely avoids to install permanent magnets on the entire secondary[17]. As a result, only the running section of the linear FSPMM experiences strong electromagnetic force, and the use of permanent magnet can be effectively cut down.

However, the continuous rise of the price of rare earth raw material in recent years has limited the promotion and application of permanent magnet machines to a large extent. For this reason, electrically-excited and hybrid-excited machines have come back to the sight of scholars and engineers[18]-[21]. In addition, the electrical excitation further enhances the speed adjustment performance[22] and completely prevents the demagnetisation issue. For electrically-excited flux-switching machines (EEFSMs), the iron core can be made as an integrated structure[23][24], instead of the common C-type or E-type modular iron core in the permanent magnet machines[25][26], which provides great convenience and reliability in the assembling process. On the other hand, the critical weakness of the electrically-excited flux-switching machine is that the torque density/thrust density is much lower than that of the permanent magnet type. Large currents or more turns of wires are required to provide equivalent magnetic energy to the permanent magnets like NdFeB and SmCo. Furthermore, the magnetic saturation in stator teeth wounded by field coils could be another reason for the low torque density/thrust density[27].

To overcome the limitation in torque density/thrust density, [28] proposed a dual-stator flux-switching structure in which the field and armature windings were separately installed on the inner and outer stators. This design made the most use of the space in the electrical machine and thus could achieve higher torque density compared with the conventional structure. [29] deduced the relationship between the field and armature

currents and developed corresponding control strategy for realising the maximum torque in a 14p/24s outer-rotor machine for traction applications. [30] applied a machine topology with non-overlapping winding and segmented rotor to achieve short magnetic path and improved electromagnetic performance. [31] proposed a complementary dual-mover structure with parallel magnetic paths to achieve maximum ratio of thrust force and thrust fluctuation.

Developing high power density electrical machine system has become a major trend in the discipline of electrical engineering, and one of the main challenges is to make the most use of materials and space to achieve the upmost design. One of essential techniques to overcome the challenge is to make multi-physical analysis and take various factors into consideration[32]. For EEFSMs, there exist strong coupling between the electromagnetic and thermal performance, which are much more remarkable in contrast with surface-mounted permanent magnet machines and FSPMMs. In particular, the field winding, armature winding and iron core all need to occupy certain space in the primary, which leads to a fierce competition. Therefore, it is necessary to carry out multi-physical analyses with acceptable accuracy and

efficiency to achieve the upmost design of EEFSMs.

For above consideration, electromagnetic-thermal coupled analyses and joint optimization are carried out in this paper, to enhance the thrust performance EEFSLMs. The improved EEFSLMs can be widely used in new energy field, for example, used for producing the components of electric vehicle with higher efficiency and better reliability during the punching, painting and assembling processes.

The structure of this paper is arranged as follows. Section II introduces the topology of the target EEFSLM and its working principle. Section III elaborates the full steps of the electromagnetic-thermal joint optimisation. Section IV states the key settings of the electromagnetic and thermal modelling work. Section V makes a comprehensive comparison between the optimised designs obtained by the conventional fixed copper loss method and the proposed joint optimisation method. Section VI further investigation the influence of unequal field/armature coil sizes, as a part of the joint optimisation. Section VII uses the prototype test results to validate the electromagnetic and thermal simulation. Section VIII concludes the main work and the main findings of this paper.
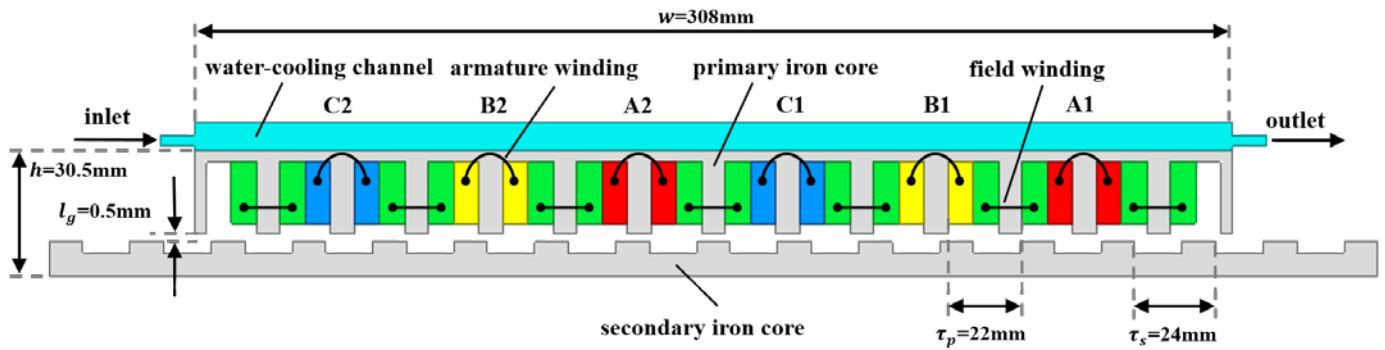

Fig. 1 Topology and fixed design parameters of EEFSLM.

II. Machine Topology and Working Principle

The EEFSLM topology studied in this paper is shown Fig. 1. The armature and field windings are alternatively wounded on the primary tooth. The main function of the secondary is to provide desired magnetic path. The primary length is designed to be 78% of the secondary length.

The EEFSLM has an 11p/12s structure, as such pole-slot combination can give higher thrust force and smaller thrust fluctuation compared with other common 12-slot options[33]. In addition, it will results in a concentrated winding arrangement, which effectively shorten the winding end length and simplify the winding mounting process. To deal with three-phase unbalance issue caused by the asymmetrical distribution of the field coils, the EEFSLM is equip with a total of 7 field coils and 6 armature coils. Both the primary and secondary have an integrated iron core structure, which completely avoids the assembly difficulties led by modular cores.

A water-cooling channel is arranged on the back of the primary yoke. To make the cooling structure simple and reliable, the cooling channel is made to be one-way. The rated cooling flow rate is 600L/h.
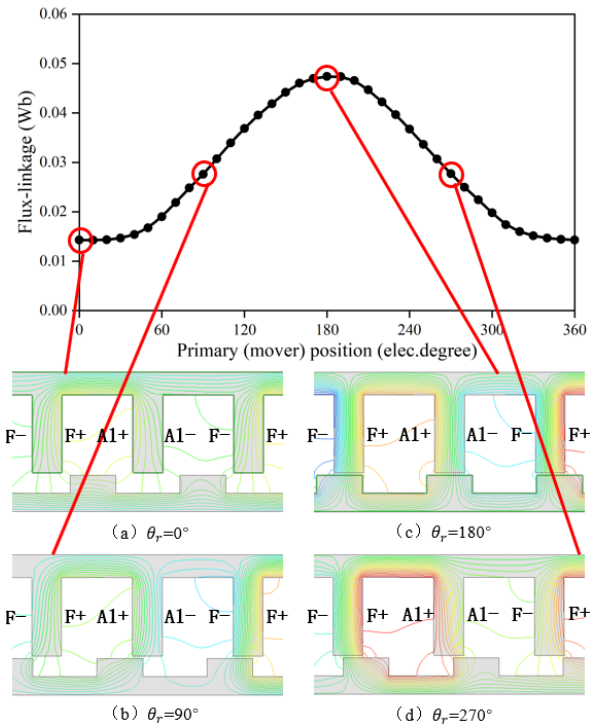

Fig. 2 Flux linkage waveform of EEFSLM.

The working principle of the EEFSLM, which observes the rule of minimum reluctance[34], can be described with the aid of the flux linkage waveform shown in Fig. 2. When the centreline of the armature coil A1 is aligned with the centreline of the secondary slot, the flux linkage reaches its minimum; when the centreline of the armature coil A1 is aligned with the centreline of the secondary teeth, the flux linkage reaches its maximum. With the movement of the primary, the unipolar flux linkage changes periodically and thus induces electromotive force (EMF) in the armature coil A1.

The design parameters of the EEFSLM are annotated in Fig. 1 and Fig. 3. In detail, Fig. 1 gives the geometric constraints, including the envelope dimensions and the airgap length, and Fig. 3 gives variable parameters which will be adjusted during the optimisation process. Equations (1), (2) and (3) further define the split ratio γ_{sr}, the field coil area ratio γ_{fsa}, and the field winding copper loss ratio γ_{fcl} respectively. Table I gives the initial values of the design parameters which are regarded as the starting point of the joint optimisation.
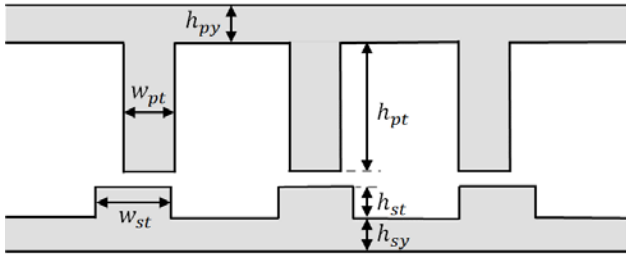

Fig. 3. Variable design parameters of EEFSLM.

$$\gamma_{sr} = \frac{h_{pt} + h_{py}}{h_{pt} + h_{py} + l_g + h_{st} + h_{sy}} \tag{1}$$

where h_{pt} and h_{py} are the primary tooth height and yoke height, h_{st} and h_{sy} are the secondary tooth height and yoke height, and l_g is the airgap length.

$$\gamma_{fsa} = \frac{s_f k_f}{s_f k_f + s_a k_a} \tag{2}$$

where S_f and S_a are the areas of the field coil and armature coil in an individual primary slot, k_f and k_a are the corresponding slot filling factors with a fixed value of 0.45.

$$\gamma_{fcl} = \frac{P_{cuf}}{P_{cuf} + P_{cua}} \tag{3}$$

where P_{cuf} and P_{cua} are the copper losses of the field winding and armature winding respectively.

TABLE I
INITIAL DESIGN PARAMETERS OF EEFSLM

Parameter	Value
Primary tooth width, w_{pt}	7mm
Primary tooth height, h_{pt}	21.35mm
Primary yoke height, h_{py}	3.5mm
Primary pole pitch, τ_p	22mm*
Airgap length, lg	0.5mm*
Secondary tooth width, w_{st}	10mm
Secondary tooth height, h_{st}	3.15mm
Secondary yoke height, h_{sy}	7mm
Secondary pole pitch, τ_s	24mm*
Stack length, l_δ	30mm*

Symbol* indicates that the parameter has a fixed value

III. JOINT OPTIMISATION METHOD

To carry out motor design and optimisation, it is necessary to give certain constraints. A common approach is to define reasonable current density or loss limit to prevent the electrical machines from overheating. Moreover, in the cases that the copper loss dominates, the fixed copper loss method (FCLM) is widely adopted[9][25][35]. This method does consider the thermal impact to some extent, as it essentially presumes that the temperature rise does not change significantly if the envelop dimensions remain the same. However, the FCLM might fail to achieve optimum design for water-cooled EEFSLMs owing to two factors:

(1) The performance of water cooling is much better than that of natural cooling, so the convection thermal resistance between the primary yoke and the cooling medium will be small. In other words, the main temperature gradient will appear in the stator slot. In this condition, the distribution of heat source (i.e., copper loss) in the primary slot will have prominent influence on the temperature rise of the windings.

(2) Since the field and armature coils are allocated in one primary slot, the distribution of current between these coils will affect electromagnetic performance and thermal performance simultaneously, even if the total copper loss is fixed. This is exactly the main challenge of the electromagnetic-thermal coupling analysis and joint optimisation.

To deal with the limitation of the FCLM, a multi-step electromagnetic-thermal joint optimisation method is proposed, which first ensures the consistency between the electromagnetic and thermal modelling and then considers the effect of different field/armature coil sizes. The complete procedures are illustrated in Fig. 4.
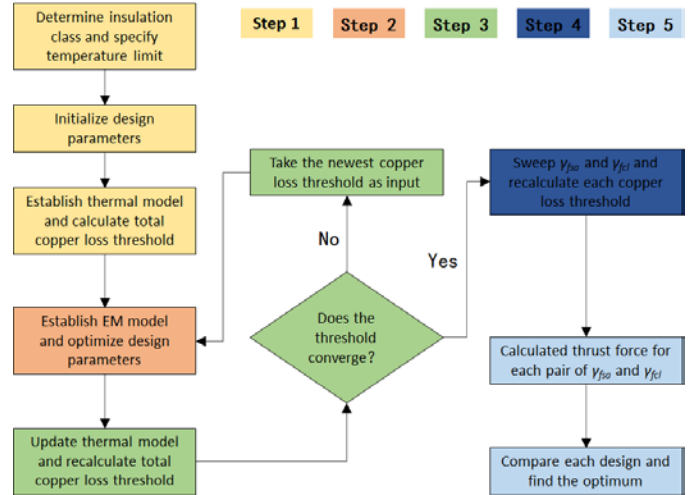

Fig. 4. Flowchart of electromagnetic-thermal joint optimisation.

Step 1: Establish the thermal model with initial design parameters and calculate the total copper loss threshold according to the given insulation class

Step 2: Establish the electromagnetic (EM) model with the same initial parameters and optimise the parameters based on the calculated total copper loss threshold from Step 1

Step3: Make the consistency between the thermal and EM models, by updating the thermal model with the EM optimised

geometric parameters and taking the calculated total copper loss threshold as the input of the EM model

Step 4: Adjust the field coil area ratio γ_{fsa} and the field winding copper loss ratio γ_{fcl} simultaneously, then derive the corresponding field and armature copper loss thresholds

Step 5: Update the EM model in Step 3 with each group of winding parameters specified in Step 4, then derive final optimum design

It should be pointed out that the γ_{fsa} and γ_{fcl} are maintained with a fixed value of 0.5 in Steps 1&2. These values can give the largest thrust force when the magnetic saturation is not considered, according to the derivation in [27][35]. To guarantee the accuracy of the electric resistance, average temperatures for the field winding and armature winding are also updated in each round of Step 3. The iterative update in Step 3 is ceased when the difference of the maximum winding temperature between two iteration is smaller than 2°C. Furthermore, Steps 1&2 are exactly the FCLM, whereas Steps 3-5 are the main contributions of this paper.

IV. ELECTROMAGNETIC AND THERMAL MODELLING

A. Electromagnetic Model

The EM simulation is based on two-dimensional finite element (FE) model to save computational resource. Both the primary and secondary iron cores are made of 50WW470 silicon steel sheets. Both the field and armature coils are made of copper wires with a diameter of 0.6mm. The change of electric resistance with temperature is considered by (4).

$$R = \left[1 + \alpha\left(T - 20\right)\right]R_{20} \tag{4}$$

where R is the winding resistance at certain operating temperature, T is the average winding temperature calculated from the thermal model, α is the temperature coefficient of resistance, and R_{20} is the winding resistance at 20°C.

In order to investigate the influence of insulation class on the optimisation, the E-, F- and H-class insulations are selected to represent different temperature limits for the EEFSLM.

B. Thermal Model

To keep the consistency between the EM and thermal simulations, two-dimensional CFD model is adopted for thermal analysis. The water-cooling channel is built in the CFD model to represent the conjugate heat transfer. The cooling water has an inflow temperature of 15°C and travels at a constant speed of 0.35m/s. The other exposed boundaries in the CFD model are specified by a fixed heat transfer coefficient of 10W/m²K, which represents the effect of natural convection.

TABLE II
MATERIAL PROPERTIES IN CFD MODEL

Component/Material	Density kg/m3	Thermal conductivity W/(m·K)	Heat Capacity J/(kg·K)
Field winding	3100	0.28	480
Armature winding	3100	0.28	480
Primary iron core	7600	35	460
Secondary iron core	7600	35	460
Airgap	1.06	0.029	1017
Cooling water	998.2	0.6	4182

The material property settings in the CFD model are listed in Table II. It should be pointed out that the thermal properties of both field and armature windings are defined with equivalent values, which are derived according to the slot filling factors and the composition of the wires.

V. OPTIMISATION WITH EQUAL FIELD/ARMATURE COIL SIZE

A. Influence of Design Parameters on Thrust Force

Based upon the initial design parameters given in Table I, the total copper loss threshold and the winding temperatures can be calculated from the CFD model. The results for each insulation class are displayed in Table III

TABLE III
INITIAL COPPER LOSS THRESHOLD AND WINDING TEMPERATURE

	E-class	F-class	H-class
Maximum winding temperature	120.0°C	155.0°C	180.0°C
Average field winding temperature	71.4 °C	90.2 °C	103.7 °C
Average armature winding temperature	77.5 °C	98.3 °C	113.2 °C
Total copper loss threshold	101.0W	134.8W	159.0W

Taking the total copper loss threshold as constraint, sequential optimisation is carried out with respective to several chosen parameters, viz. split ratio, primary tooth width, primary yoke height, secondary tooth width and secondary tooth height.

It is found that the thrust force is the most sensitive to the variation of the split ratio, as indicated by Fig. 5. Nevertheless, whatever the insulation class is, the optimal split ratio always lies in a narrow range (i.e., 0.75~0.77).

It is further found that choosing suitable primary tooth width is of secondary importance for large thrust force. According to the results shown in Fig. 6, the higher class of insulation entails wider primary tooth width, to alleviate the magnetic saturation at the primary iron core caused by the augmented field and armature currents.
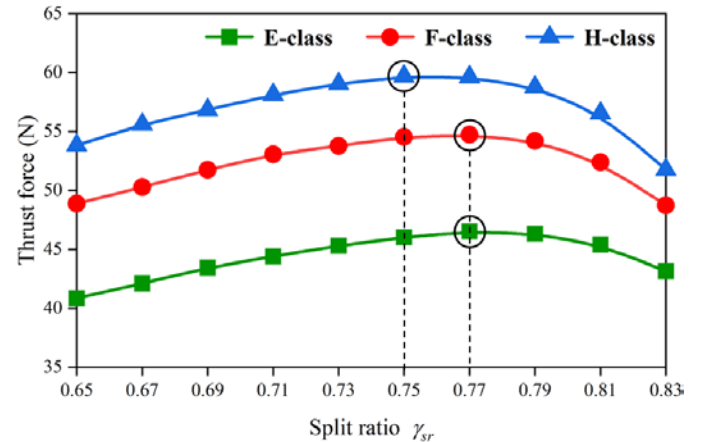

Fig. 5. Variation of thrust force with split ratio.

B. Optimised Design by Fixed Copper Loss Method

Referring to the sensitivity of the parameters, consequential optimisation is carried out to seek the high thrust design. After taking 3 rounds of iteration, the thrust force of the EEFSLM gets stable. The optimised design parameters are given in Table IV. It can be noted that the higher class of insulation leads to
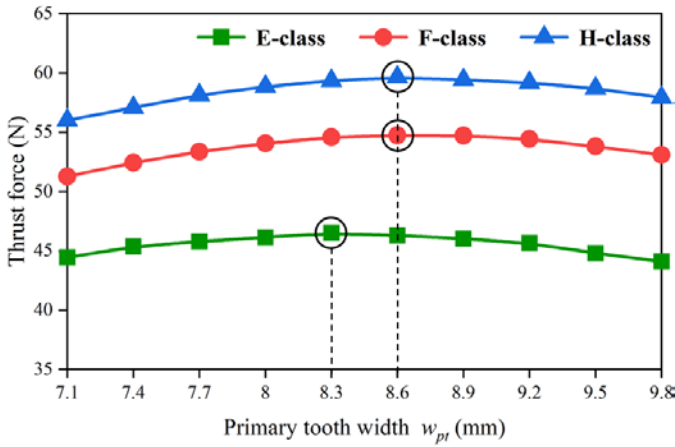
Fig. 6. Variation of thrust force with primary tooth width.

larger size of the optimised primary tooth width, primary yoke height and secondary yoke height. This is also accommodated to alleviate the magnetic saturation caused by the augmented field and armature currents.

TABLE IV
OPTIMISED DESIGN PARAMETERS BY FCLM

Parameter	Value		
	E-class	F-class	H-class
Split ratio, γ_{sr}	0.77	0.77	0.75
Primary tooth width, w_{pt} (mm)	8.3	8.6	8.7
Primary tooth height, h_{pt} (mm)	23.19	22.95	22.19
Primary yoke height, h_{py} (mm)	4.15	4.39	4.44
Primary yoke height / primary tooth width, h_{py} / w_{pt}	0.5	0.51	0.51
Secondary tooth width, w_{st} (mm)	9.4	9.3	9.1
Secondary tooth height, h_{st} (mm)	4.09	3.94	4.55
Secondary yoke height, h_{sy} (mm)	3.57	3.72	3.82
Secondary yoke height / secondary tooth width, h_{sy} / w_{st}	0.38	0.40	0.42
Thrust force, F_{avg} (N)	**46.5**	**54.7**	**59.7**

The genetic algorithm is adopted as an alternative of the sequential optimisation method, for the purpose of validation. Comparing the results in Fig. 7 with those in Table IV, the improvements made by the genetic algorithm are only 0.13%, 0.20% and 0.34% for E-, F- and H-class insulation respectively. Thus, it can be confirmed that the sequential optimisation results are reliable, while the genetic algorithm takes much more iterations.
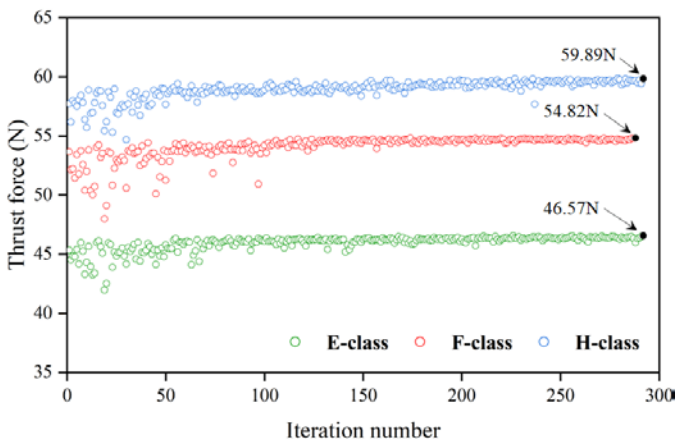

Fig. 7. Optimisation history based on genetic algorithm.

C. Optimised Design by Joint Optimisation

After updating the thermal model with the geometric parameters mentioned in Table IV, it is found that the maximum winding temperatures for E-, F- and H-class insulation are only 108.8°C, 134.7°C, 152.2°C respectively, which are far from their limits. This evident clearly indicates the limitation of the FCLM. Therefore, joint optimisation is carried out to maintain the consistency between the electromagnetic and thermal models. The current joint optimisation takes 2 rounds of iteration between the two models.

The design parameters obtained by the joint optimisation method are given in Table V. Compared with the FCLM results in Table IV, the joint optimisation makes more than 5% increase of thrust force for all the insulation. It can be further found that the sizes of primary tooth width, secondary tooth width and secondary yoke height are even larger in Table V, again, to accommodate the increased magnetic load.

TABLE V
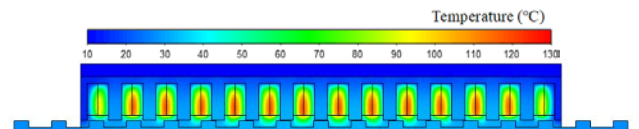OPTIMISED DESIGN PARAMETERS BY JOINT OPTIMISATION

Parameter	Value		
	E-class	F-class	H-class
Split ratio, γ_{sr}	0.77	0.77	0.75
Primary tooth width, w_{pt} (mm)	8.3	8.8	8.9
Primary tooth height, h_{pt} (mm)	23.02	22.76	22.00
Primary yoke height, h_{py} (mm)	4.32	4.58	4.63
Primary yoke height / primary tooth width, h_{py} / w_{pt}	0.52	0.52	0.52
Secondary tooth width, w_{st} (mm)	9.4	9.3	9.2
Secondary tooth height, h_{st} (mm)	4.09	3.95	4.42
Secondary yoke height, h_{sy} (mm)	3.57	3.72	3.96
Secondary yoke height / secondary tooth width, h_{sy} / w_{st}	0.38	0.40	0.43
Thrust force, F_{avg} (N)	**50.7**	**59.9**	**64.4**
Total copper loss threshold, $P_{cuf} + P_{cua}$ (W)	**113.6**	**153.1**	**177.4**

VI. ADDITIONAL OPTIMISATION CONSIDERING UNEQUAL FIELD/ARMATURE COIL SIZES

In previous research work, the field and armature coils are always presumed to have the same size. However, different field/armature coil sizes accompanied with uneven current loads can be a possible solution for much better cooling performance. As a result, the thrust density might be improved for the same temperature limit. For this consideration, this section makes a comprehensive study of the combination of the field coil area ratio γ_{fsa} and the field winding copper loss ratio γ_{fcl} referring to the parameters given in in Table V.

A. Influence of Field/armature Coil sizes and Copper Losses on Temperature

Taking E-class insulation case as an example, the temperature distributions for three different cases are given in Fig. 8(a)-(c). The very different temperature fields can be observed. It should be emphasised that the total copper loss is maintained to be unchanged across the three cases.

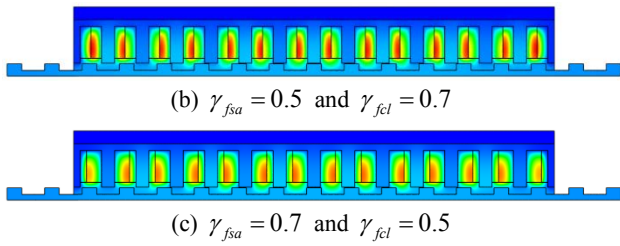(a) $\gamma_{fsa} = 0.5$ and $\gamma_{fcl} = 0.5$

WEN et al. : ELECTROMAGNETIC-THERMAL COUPLED ANALYSES AND JOINT OPTIMISATION OF ELECTRICALLY-EXCITED
FLUX-SWITCHING LINEAR MACHINES

373

(b) $\gamma_{fsa} = 0.5$ and $\gamma_{fcl} = 0.7$

(c) $\gamma_{fsa} = 0.7$ and $\gamma_{fcl} = 0.5$

Fig. 8 Temperature distributions under the same total copper loss.

Fig. 9 Heat flow paths in the primary of EEFSLM

In the case of identical field/armature coil size correspond to Fig. 8a, more than 98% of the generated copper loss are brought away by the cooling water. The temperature distributions in the field and armature coils are slightly asymmetrical. The highest temperature is 120°C, occurring on the armature winding and near the junction of two adjacent coils, since the heat source density of each armature coil is even higher. The maximum temperature of the field winding is slightly lower, as to be 113.4°C. The interface between the primary yoke and the water-cooling channel is 22.5°C in average, which evinces large temperature gradient inside each slot of the primary. The temperature in the two lateral slots is significantly lower, because these slots only hold the field coils.

With the increase of the field winding copper loss ratio γ_{fcl}, the more concentrated heat source induces a significant raise temperature in all the field coils. As shown in Fig. 8b, the maximum temperature of the field winding is raised from 113.4°C to 130°C, whereas the maximum temperature of the armature winding is decreased from 120°C to 99.8°C. Such hotspot effect is very detrimental to the insulation lifetime.

With the increase of the field coil area ratio γ_{fsa}, the heat source in any armature coil becomes more concentrated than before, but the heat transfer path becomes shorter. As a consequence, the temperature of the armature winding is effectively reduced by 20.6°C, as can be observed from in Fig. 8c. Meanwhile, for any field coil, the heat source density declines and the heat transfer area is increased at the position of slot bottom, but the heat transfer path becomes longer. As a result, the temperature of the field winding is slightly increased, as from 113.4°C to 116.2°C.

According to the above findings, total copper loss threshold can be broken by finding suitable γ_{fcl} and γ_{fsa} combination. Hence, it is also possible to achieve improved thrust force with higher current loads. For this consideration, it is determined to make a rough theoretical analysis at first, with the aid of thermal network. The thermal network is schematically shown in Fig. 9. The generated copper loss in any coil can be transfer via two main paths. It is further assumed that there is no heat transfer between the field coil and the armature coil in the same slot. This assumption is based on the fact that there is always a gap between the two adjacent coils which acts as a good isothermal layer. In this case, the thermal network can be divided into two isolated parts, and individual copper loss threshold can be easily calculated.

In a primary slot, the width of the field coil is varied as Δ, while the total width of the field and armature coils is held. By making this adjustment, it is equivalent to parametrise the field coil area ratio γ_{fsa}. The calculated results are given in Fig. 10,
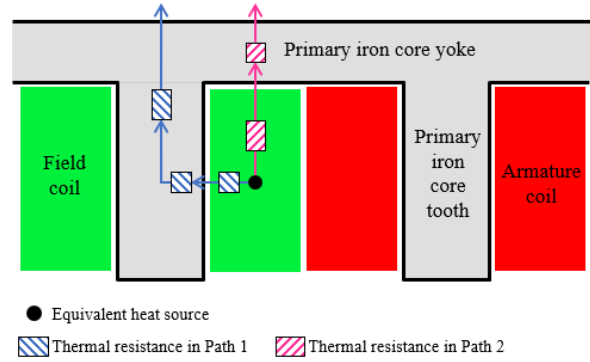
the smaller size of either coil can withstand more copper loss. In addition, the very different sizes between the field and armature coils seems to be favourable for high total copper loss threshold.
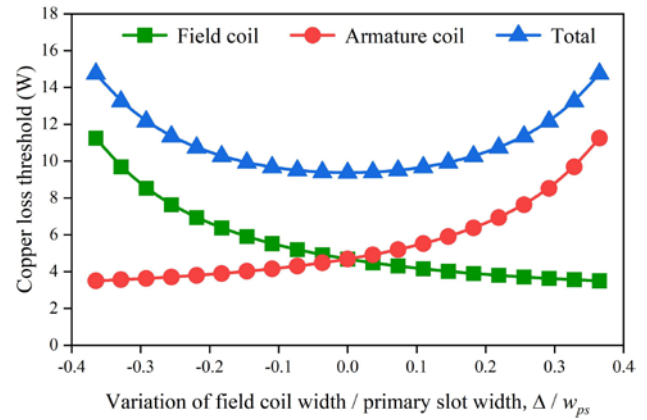

Fig. 10 Varied copper loss threshold with field/armature coil size.

B. Influence of Field/armature Coil Sizes and Copper Losses on Thrust Force

Total copper loss threshold is calculated for different combinations of the field winding copper loss ratio γ_{fcl} and the field coil area ratio γ_{fsa}, based on the CFD model. The results for the E-class insulation case are displayed in Fig. 11. In general, the data exhibit a saddle-like distribution.

For a fixed γ_{fsa}, the total copper loss threshold always increases with the γ_{fcl} first and then decreases. For an increased γ_{fsa}, a smaller γ_{fcl} value is always required to reach the local optimum. In addition, the larger area difference is, the higher threshold can be achieved, which agrees with the finding in the theoretical analysis. The black dot in Fig. 11 represents the initial combination of γ_{fsa}=0.5 and γ_{fcl}=0.5 This combination results in lower total copper loss threshold compared with the adjacent optimums. The results for the F- and H-class are not shown here, since the distributions also reveal a saddle-like shape similar to that in Fig. 11.

Substituting the derived total copper loss threshold for each combination of γ_{fcl} and γ_{fsa} into the EM model, the thrust force under the 120°C temperature limit can be calculated. The results are displayed in Fig. 12, corresponding to the E-class insulation as well. The data in the figure exhibit an elliptical parabolic distribution. The thrust force reaches the global maximum when γ_{fsa}=0.6 and γ_{fcl}=0.47, which is 4.5% higher than the initial combination of γ_{fsa}=0.5 and γ_{fcl}=0.5 (black dot in
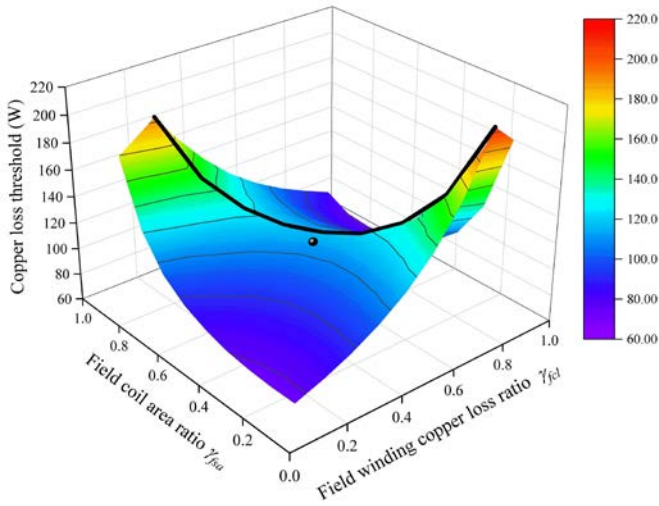
Fig. 11. Variation of total copper loss threshold with γ_{fcl} and $\gamma_{fsa.}$

the Fig. 12). According to this finding, it can be deduced that the combination of relatively large size of field coil and relatively low field copper loss is favourable for achieving high thrust force for the current EEFSLM design.
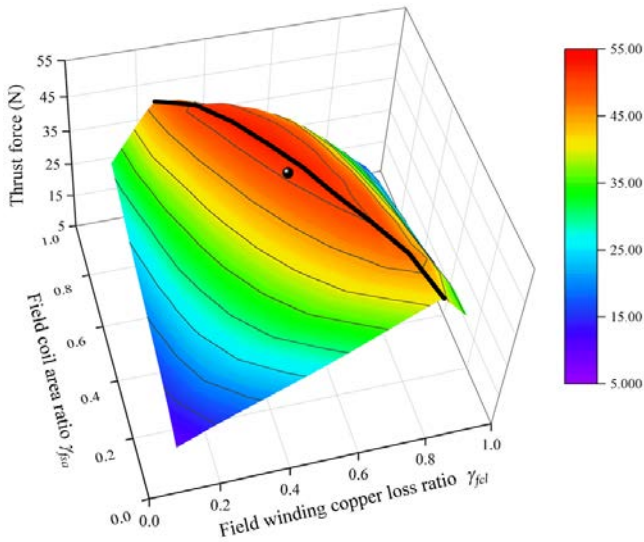

Fig. 12. Variation of thrust force with γ_{fcl} and $\gamma_{fsa..}$

C. Comparison of Different Optimisation Methods

Fig. 13 displays the optimum thrust forces of the EEFSLM obtained by different optimisation methods. In these methods, the FCLM corresponds to Steps 1&2 given in Fig. 4, and the joint optimisation methods for identical field/armature coil size and unequal field/armature coil size corresponds to Steps 1-4 and Steps 1-5 respectively. Compared with the conventional FCLM, the electromagnetic-thermal joint optimisation brings much higher average thrust force. The improvements for E-, F- and H- class insulation are 13.4%, 15.1%, 13.3% respectively.

Fig. 14 further displays the total copper loss thresholds. It can be seen that the FCLM under-estimates the threshold for all the insulation classes, stemming from the change of primary core and slot geometries during the optimisation process. The specific combination of unequal field/armature coil sizes and field/armature copper losses, namely γ_{fsa}=0.6 and γ_{fcl}=0.47, leads to further increase of total copper loss threshold.
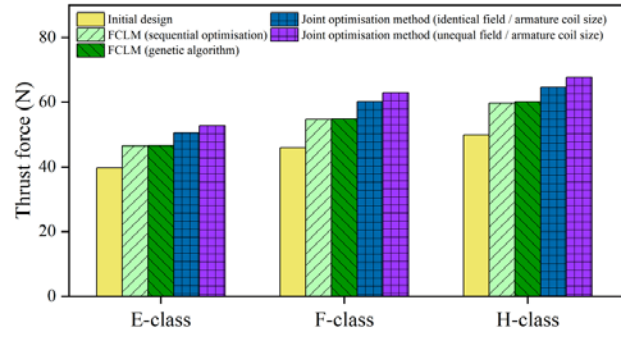

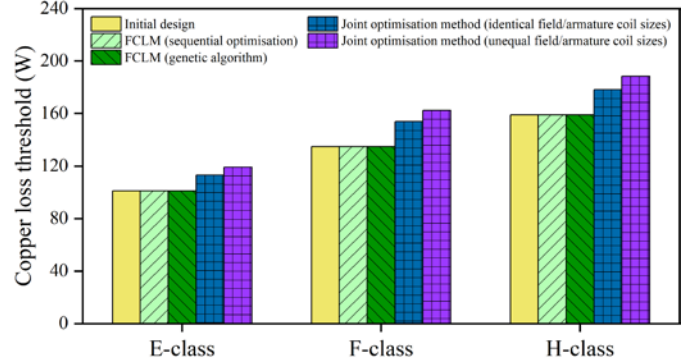Fig. 13. Optimum thrust forces by different optimisation methods.

Fig. 14. Copper loss thresholds by different optimisation methods.

The above improvement made by the joint optimisation can be attributed to two factors. First, the joint optimisation ensures the consistency between the electromagnetic model and the thermal model, by means of updating the geometric information, the field/armature copper loss thresholds and the average winding temperatures iteratively. Second, the joint optimisation considers the effect of unequal field/armature coil sizes and derives more suitable copper loss distribution, while the conventional FCLM totally ignores the influence of heat source distribution on the temperature field and local hotspots.

VII. EXPERIMENTAL VALIDATION

An 11p/12s EEFSLM prototype was manufactured to test and verify the EM and thermal performance. Its appearance is exhibited in Fig. 15. The envelope dimensions of the prototype are the same as those studied before, while the slot size and the number of coil turns are different from before, due to the convenience of manufacturing. The detailed parameters of the prototype are given in Table VI.
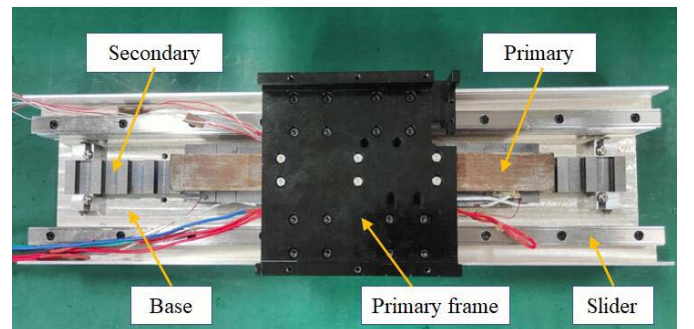

Fig. 15 EEFSLM prototype.

TABLE VI
PARAMETERS OF EEFSLM PROTOTYPE

Parameter	Value
Primary tooth width, w_{pt}	8.3mm
Primary tooth height, h_{pt}	23mm
Primary yoke height, h_{py}	9.3mm
Primary pole pitch, τ_p	22mm
Airgap length, lg	0.5mm
Secondary tooth width, w_{st}	9.4mm
Secondary tooth height, h_{st}	4.1mm
Secondary yoke height, h_{sy}	8.6mm
Secondary pole pitch, τ_s	24mm
Stack length, l_δ	30mm
Primary speed, v	0.3m/s
Number of field coil turns / wire diameter	264 turns / 0.59mm
Number of armature coil turns / wire diameter	113 turns / 0.59mm
Field current	0.92A

By making the use of the back-to-back test rig illustrated in Fig. 16, the back-EMF of the prototype was measured under an open-circuit condition. The results in Fig. 17 suggest good consistency between the modelling results and the experimental measurements. Thus, the EM performance is validated.
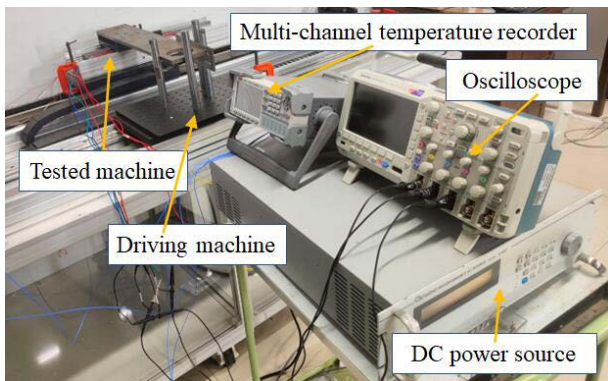

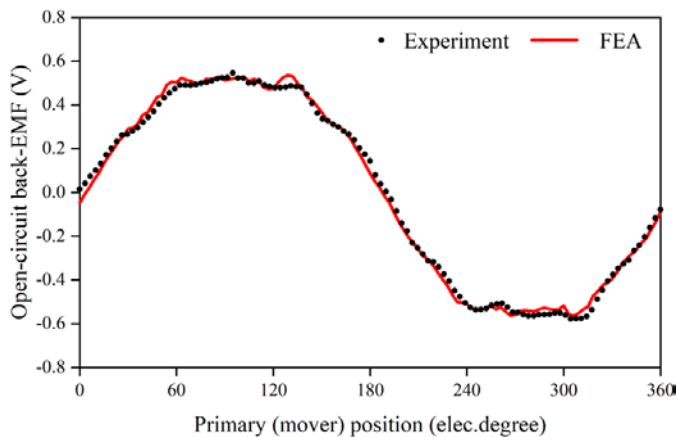
Fig. 16 Back-to-back test rig for linear machines.

Fig. 17. Back-EMF waveforms.

In order to validate the thermal performance, three PT100 temperature sensors were embedded into 1 field coil and 2 armature coils when these coils had been wounded. The positions of the PT100s are roughly indicated in Fig. 18. DC currents of 1.39A and 1.33A were continuously applied to the field winding and the armature winding, and until the steady-state for temperature rise was achieved.

As can be noted from the results in Fig. 19, the thermal model successfully realises the characteristic that the field winding has higher temperature than the armature winding. The results indicate excellent accuracy of the thermal simulation, since the temperature difference between the experiment and the simulation is within 5% for all the three positions.
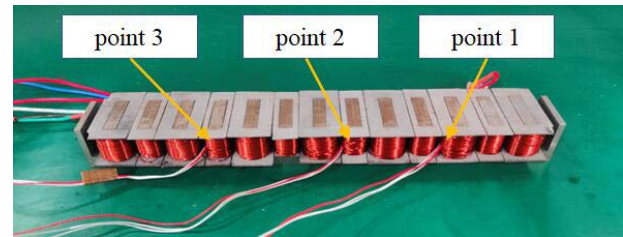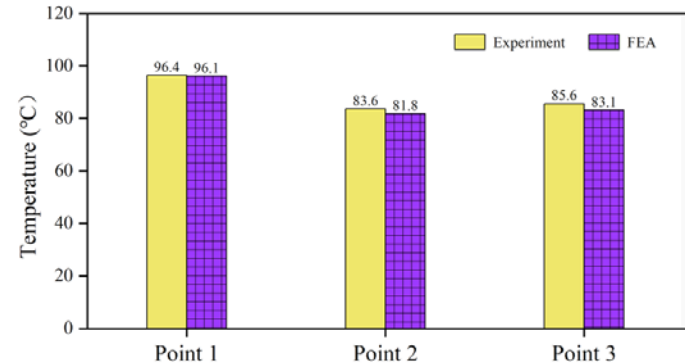

Fig. 18 Positions of PT100 temperature sensors.

Fig. 19 Winding temperatures under steady-state condition.

VIII. CONCLUSIONS

In this paper, water-cooled EEFSLMs, which can be used for intelligent manufacturing purpose in the field of new energy technology, are investigated to achieve high thrust performance. By using the conventional FCLM, it is found that the split ratio and the primary tooth width have the most significant impact on the thrust force. Nevertheless, the FCLM is proven to be no longer suitable for the high thrust density design of the water-cooled EEFSLMs, since it is unable to fully consider the strong coupling between the electromagnetic and thermal performance. Moreover, for the EEFSLMs in this paper, the reliability of the FCLM is critically hinged on the copper loss threshold derived from initial design parameters.

To overcome the limitation of the FCLM, a multi-step electromagnetic-thermal joint optimisation method is proposed. It ensures the consistency between the electromagnetic and thermal modelling and further considers the effect of different field/armature coil sizes.

By using the proposed optimisation method, it is found that the very different sizes between the field and armature coils is essential for total copper loss threshold. On the other hand, the combination of relatively large size of field coil and relatively low field copper loss is favourable for achieving high thrust force for the current EEFSLM under the temperature limit condition. For the E-class insulation, the thrust force reaches the global maximum when the field coil area ratio γ_{fsa}=0.6 and the field winding copper loss ratio γ_{fcl}=0.47. The thrust force is further improved by 13-15% compared with the FCLM for all the insulation classes, which manifests the superiority of the proposed joint optimisation method.

A prototype of the EEFSLM is manufactured to verify the electromagnetic and thermal performance. The simulation results agree well with the measured back EMF waveform and the measured temperature at three positions.

REFERENCES

[1] Z. Q. Zhu and J. T. Chen, "Advanced flux-switching permanent magnet brushless machines," *IEEE Trans. Magn.*, vol. 46, no. 6, pp. 1447-1453, Jun. 2010.

[2] M. Cheng, G. Zhang and W. Hua, "Overview of stator permanent magnet brushless machine systems and their key technologies," *Proceedings of the CSEE*, vol. 34, no. 29, pp. 5204-5220, Oct. 2014.

[3] X. Zhu, Z. Shu, L. Quan, Z. Xiang and X. Pan, "Design and multicondition comparison of two outer-rotor flux-switching permanent-magnet motors for in-wheel traction applications," *IEEE Trans. Ind. Electron.*, vol. 64, no. 8, pp. 6137-6148, Aug. 2017.

[4] Z. Q. Zhu, "Novel switched flux permanent magnet machine topologies," *Transactions of China Electrotechnical Society*, vol. 27, no. 7, pp. 1-16, Apr. 2012.

[5] L. Wu, J. Zhu and Y. Fang, "A novel doubly-fed flux-switching permanent magnet machine with armature windings wound on both stator poles and rotor teeth," *IEEE Trans. Ind. Electron.*, vol. 67, no. 12, pp. 10223-10232, Dec. 2020.

[6] W. Li and M. Cheng, "Reliability analysis and evaluation for flux-switching permanent magnet machine," *IEEE Trans. Ind. Electron.*, vol. 66, no. 3, pp. 1760-1769, Mar. 2019.

[7] P. Su, W. Hua, Z. Wu, P. Han and M. Cheng, "Analysis of the operation principle for rotor-permanent-magnet flux-switching machines," *IEEE Trans. Ind. Electron.*, vol. 65, no. 2, pp. 1062-1073, Feb. 2018.

[8] P. Wang, W. Hua, G. Zhang, B. Wang and M. Cheng, "Principle of flux-switching PM machine by magnetic field modulation theory Part II: Electromagnetic torque generation," *IEEE Trans. Ind. Electron.*, vol. 69, no. 3, pp. 2437-2446, Mar. 2022.

[9] L. Wu, G. Ming, L. Zhang, Y. Fang, T. Li and W. Zheng, "Comparative study between doubly salient PM machine with new stator/rotor-pole number combination and biased flux PM machine," *IEEE Trans. Ind. Appl.*, vol. 57, no. 3, pp. 2354-2365, May-Jun. 2021.

[10] J. T. Chen and Z. Q. Zhu, "Influence of the rotor pole number on optimal parameters in flux-switching PM brushless AC machines by the lumped-parameter magnetic circuit model," *IEEE Trans. Ind. Appl.*, vol. 46, no. 4, pp. 1381-1388, Jul.-Aug. 2010.

[11] J. Zhu and L. Wu, "Winding configurations and pole/tooth combinations of doubly-fed flux-switching permanent magnet machines," *IEEE Trans. Ind. Electron.*, vol. 69, no. 3, pp. 2380-2389, Mar. 2022.

[12] Q. Ding, X. Wang, Z. Deng and T. Ni, "Design and comparison of radial force winding configurations for wide air-gap flux-switching bearingless permanent-magnet motor," *Transactions of China Electrotechnical Society*, vol. 33, no. 11, pp. 2403-2413, Jun. 2018.

[13] D. J. Evans and Z. Q. Zhu, "Novel partitioned stator switched flux permanent magnet machines," *IEEE Trans. Magn.*, vol. 51, no. 1, pp. 1-14, Jan. 2015.

[14] G. Lian, B. Chen, F. Ban and G. Gu, "Study on winding combination and harmonic characteristics of flux-switching machines with segmental rotor," *Transactions of China Electrotechnical Society*, vol. 35, no. S1, pp. 136-148, Dec. 2020.

[15] G. Zhang, W. Hua, M. Cheng, B. Zhang and X. Guo, "Coupled magnetic-thermal fields analysis of water cooling flux-switching permanent magnet motors by an axially segmented model," *IEEE Trans. Magn.*, vol. 53, no. 6, pp. 1-4, Jun. 2017.

[16] H. Ding, W. Sixel, L. Zhang, A. Hembel, L. Handy-Cardenas, G. Nellis and B. Sarlioglu, "Evaluation of the self-cooling performance of a flux-switching permanent magnet machine with airfoil-shaped rotor," *IEEE Trans. Ind. Appl.*, vol. 57, no. 4, pp. 3710-3721, Jul.-Aug. 2021.

[17] Y. Shen and Q. Lu, "Overview of permanent magnet linear machines with primary excitation," *Transactions of China Electrotechnical Society*, vol. 36, no. 11, pp. 2325-2343, Jun. 2021.

[18] Z. Wu, Z. Q. Zhu, C. Wang, J. C. Mipo, S. Personnaz and P. Farah, "Analysis and reduction of on-load DC winding induced voltage in wound field switched flux machines," *IEEE Trans. Ind. Electron.*, vol. 67, no. 4, pp. 2655-2666, Apr. 2020.

[19] H. Hua, Z. Q. Zhu, W. Hua, L. Zhu, S. Jiang and X. Luo, "Investigation of partitioned stator hybrid excited switched flux machines with different rotor piece numbers," *Proceedings of the CSEE*, vol. 41, no. 16, pp. 5715-5727, Aug. 2021.

[20] X. Fu, Z. Jiang, H. Lü, S. Gu and W. Cui, "Review of the blushless excitation and torque density improvement in wound field synchronous motors," *Transactions of China Electrotechnical Society*, vol. 37, no. 7, pp. 1689-1702, Apr. 2022.

[21] B. Ullah, F. Khan, S. Hussain and B. Khan, "Modeling, optimization, and analysis of segmented stator flux switching linear hybrid excited machine for electric power train," *IEEE Trans. Transport. Electrific.*, vol. 8, no. 3, pp. 3546-3553, Sept. 2022.

[22] J. T. Chen, Z. Q. Zhu, S. Iwasaki and R. P. Deodhar, "A novel hybrid-excited switched-flux brushless AC machine for EV/HEV applications," *IEEE Trans. on Veh. Technol.*, vol. 60, no. 4, pp. 1365-1373, May 2011.

[23] W. Jiang, W. Huang, X. Lin, Y. Zhao, X. Wu, Y. Zhao, D. Dong and X. Jiang, "A novel stator wound field flux switching machine with the combination of overlapping armature winding and asymmetric stator poles," *IEEE Trans. Ind. Electron.*, vol. 69, no. 3, pp. 2737-2748, Mar. 2022.

[24] R. Cao, X. Yuan, Y. Jin and Z. Zhang, "MW-class stator wound field flux-switching motor for semidirect drive wind power generation system," *IEEE Trans. Ind. Electron.*, vol. 66, no. 1, pp. 795-805, Jan. 2019.

[25] J. Zhu, L. Wu and H. Wen, "Optimization and comparison of dual-armature flux-switching permanent magnet machines with different stator core shapes," *IEEE Trans. Ind. Appl.*, vol. 58, no. 1, pp. 314-324, Jan.-Feb. 2022.

[26] Y. Yao and Q. Lu, "Comparative study of E-core and C-core modular PM linear machines with different slot/pole combinations," *IEEE Trans. Magn.*, vol. 53, no. 11, pp. 1-7, Nov. 2017.

[27] J. T. Chen, Z. Q. Zhu, S. Iwasaki and R. Deodhar, "Low cost flux-switching brushless AC machines," in *2010 IEEE Vehicle Power and Propulsion Conference*, Lille, France, 2010, pp. 1-6.

[28] Z. Q. Zhu, Z. Z. Wu, D. J. Evans and W. Q. Chu, "A wound field switched flux machine with field and armature windings separately wound in double stators," *IEEE Trans. Energy Convers.*, vol. 30, no. 2, pp. 772-783, Jun. 2015.

[29] S. Yang, J. Zhang and J. Jiang, "Modeling torque characteristics and maximum torque control of a three-phase, DC-excited flux-switching machine," *IEEE Trans. Magn.*, vol. 52, no. 7, pp. 1-4, Jul. 2016.

[30] M. F. Omar, E. Sulaiman, M. Jenal, R. Kumar and R. N. Firdaus, "Magnetic flux analysis of a new field-excitation flux switching motor using segmental rotor," *IEEE Trans. Magn.* vol. 53, no. 11, pp. 1-4, Nov. 2017.

[31] N. Ullah, A. Basit, F. Khan, Y. A. Shah, A. Khan, O. Waheed and A. Usman, "Design and optimization of complementary field excited linear flux switching machine with unequal primary tooth width and segmented secondary," *IEEE Access*, vol. 7, pp. 106359-106371, 2019.

[32] W. Ma, "Thoughts on the development of frontier technology in electrical engineering," *Transactions of China Electrotechnical Society*, vol. 36, no. 22, pp. 4627-4636, Nov. 2021.

[33] Z. Q. Zhu and Y. J. Zhou, "Recent development in stator wound field synchronous machines," *Journal of Electrical Engineering*, vol. 10, no. 4, pp. 11-25, Oct.- Dec. 2015.

[34] W. Jiang, W. Huang, X. Jiang, D Dong, Q. Wang and X. Lin, "Winding configurations analysis and power density optimization of stator electrical excitation flux-switching machine," *Proceedings of the CSEE*, vol. 37, no. 21, pp. 6266-6277, Nov. 2017.

[35] W. Wang, L. Wu and J. Zhu, "Influence of end-winding on optimal design parameters for maximum torque of DC excited flux-switching machines," in *2019 22nd International Conference on Electrical Machines and Systems (ICEMS)*, Harbin, China, 2019, pp. 1-6.

WEN et al. : ELECTROMAGNETIC-THERMAL COUPLED ANALYSES AND JOINT OPTIMISATION OF ELECTRICALLY-EXCITED
FLUX-SWITCHING LINEAR MACHINES

377

Hui Wen (Member, IEEE) received the B.Eng. degree in architecture and built environment from University of Nottingham, Nottingham, U.K., in 2011, and the Ph.D. degree in civil and environmental engineering from University College London, London, U.K., in 2017.

From 2017 to 2020, he was a Research Associate with College of Electrical Engineering, Zhejiang University, Hangzhou, China. Since 2021, he has been a lecturer with School of Automation and Electrical Engineering, Zhejiang University of Science and Technology. His current research interests include multi-physical field analysis of electrical machines and thermal management of wind power generators.

Yufei Wang received the B.Eng. degree in electrical engineering in 2020 from Zhejiang University of Science and Technology, Hangzhou, China, where he has been working towards the M.Eng. degree in mechanical engineering.

His major research interests include innovative electromechanical structure design and its control.

Yuting Zheng (Member, IEEE) received the B.Eng. degree in electrical engineering from Southwest Jiaotong University, Chengdu, China, in 2016, and received the Ph.D. degree in electrical engineering from Zhejiang University, Hangzhou, China, in 2021.

In July 2021, she joined the School of Automation and Electrical Engineering, Zhejiang University of Science and Technology. Her current major research interest is the design and analysis of flux modulation permanent magnet machines.

Wen Zeng is currently pursuing the B.Eng degree in electrical engineering at Zhejiang University of Science and Technology, Hangzhou, China.

Her current research interest is the design and analysis of synchronous machines.

Xiao Qu received BS degree in measurement and Instrument from China Jiliang University, Hangzhou, China, in 1995, and the M.Sc. degree in electronic and communication engineering from Zhejiang University, Hangzhou, China, in 2005.

She is currently an Associate Professor with the School of Automation and Electrical Engineer, Zhejiang University of Science and Technology, Hangzhou. Her current research interest is Environmental measurement and control technology.

Jiongjiong Cai received the B.Eng. degree in electrical engineering and automation, M.Sc. degree in physics and the Ph.D. degree in electrical engineering all from the Zhejiang University, Hangzhou, China, in 2002, 2005, and 2014, respectively.

In 2016-2018, he was a Postdoctoral Researcher with Suzhou Industrial Technology Research Institute of Zhejiang University. He is currently an Associate Professor with the School of Automation and Electrical Engineer, Zhejiang University of Science and Technology, Hangzhou. His research interests include electromagnetic system design and control, direct driven mechanism, novel electromechanical structure design and its control.